

Non-Invasive and Point-Of-Care Surface-Enhanced Raman Scattering (SERS)-based Breathalyzer for Mass Screening of Coronavirus Disease 2019 (COVID-19) under 5 Minutes

Shi Xuan Leong^{1#}, Yong Xiang Leong^{1#}, Emily Xi Tan¹, Howard Yi Fan Sim¹, Charlynn Sher Lin Koh¹, Yih Hong Lee¹, Carice Chong¹, Li Shiuan Ng¹, Jaslyn Ru Ting Chen¹, Desmond Wei Cheng Pang¹, Lam Bang Thanh Nguyen¹, Siew Kheng Boong¹, Xuemei Han¹, Ya-Chuan Kao¹, Yi Heng Chua¹, Gia Chuong Phan-Quang^{1,2}, In Yee Phang², Hiang Kwee Lee¹, Mohammad Yazid Abdad^{3,4,5}, Nguan Soon Tan^{6,7}, Xing Yi Ling^{1*}

¹ Division of Chemistry and Biological Chemistry, School of Physical and Mathematical Sciences, Nanyang Technological University, Singapore, 637371, Singapore.

² Silver Factory Technology Pte. Ltd., Singapore, 169203, Singapore.

³ Infectious Diseases Research Laboratory, National Centre for Infectious Diseases, Singapore, 308442, Singapore.

⁴ Centre for Tropical Medicine and Global Health, Nuffield Department of Medicine, University of Oxford, Oxford, OX3 7LG, UK.

⁵ Faculty of Tropical Medicine, Mahidol University, Bangkok, 10400, Thailand.

⁶ Lee Kong Chian School of Medicine, Nanyang Technological University, Singapore, 308232, Singapore.

⁷ School of Biological Sciences, Nanyang Technological University, Singapore, 637551, Singapore.

These authors contributed equally.

* To whom correspondence should be addressed. Email: xyling@ntu.edu.sg

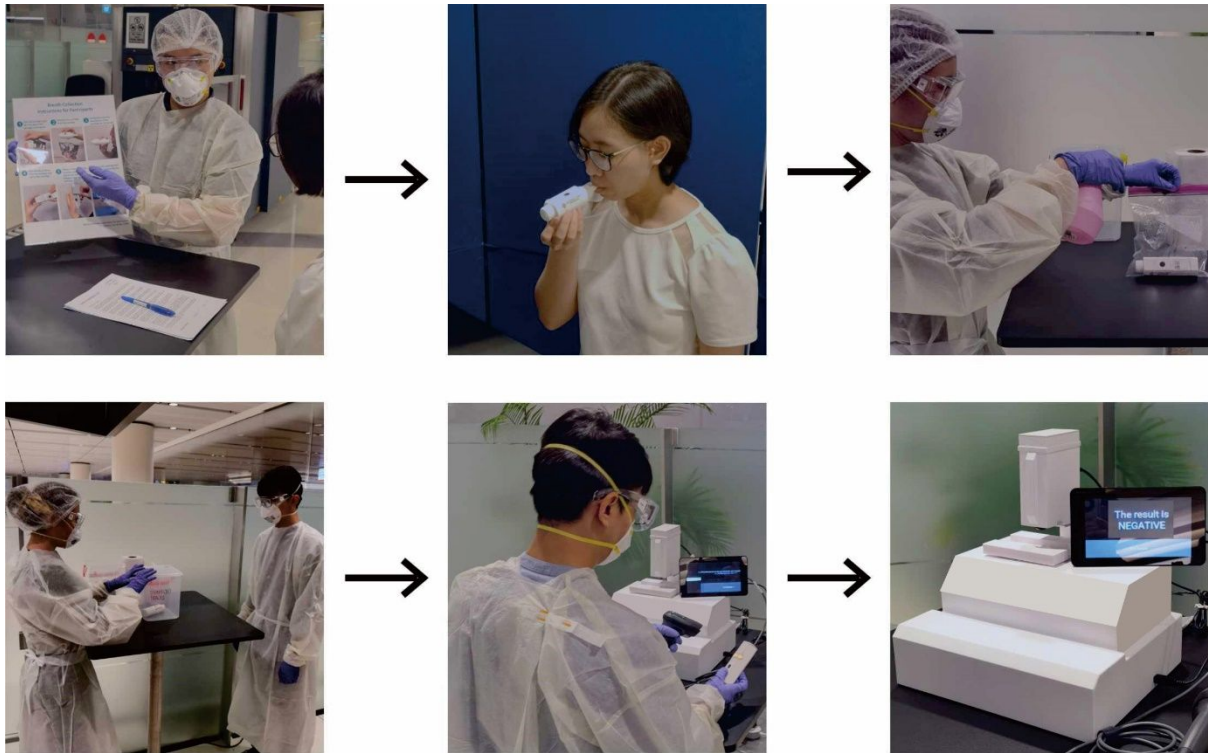


Figure S1. Digital images describing the participant recruitment workflow, which includes briefing the participant, breath sample collection, breathalyzer disinfection, SERS measurement and obtaining the prediction outcome.

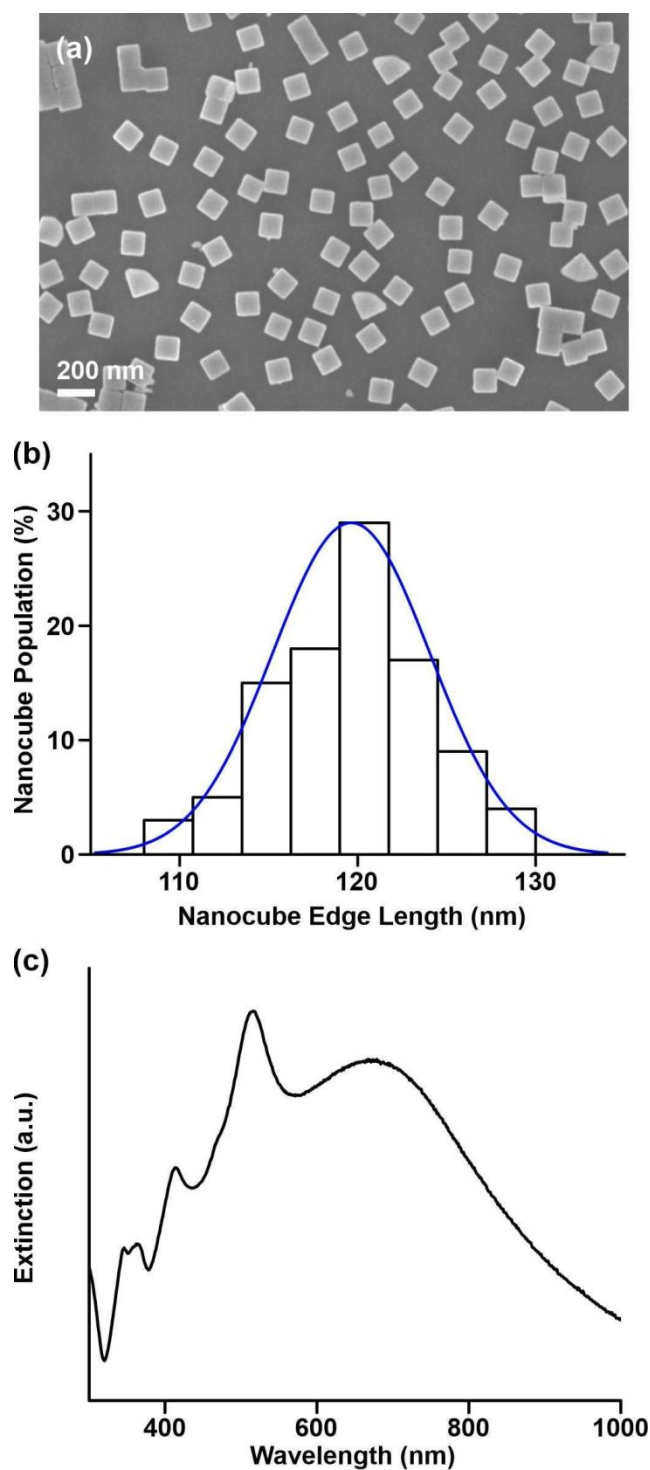
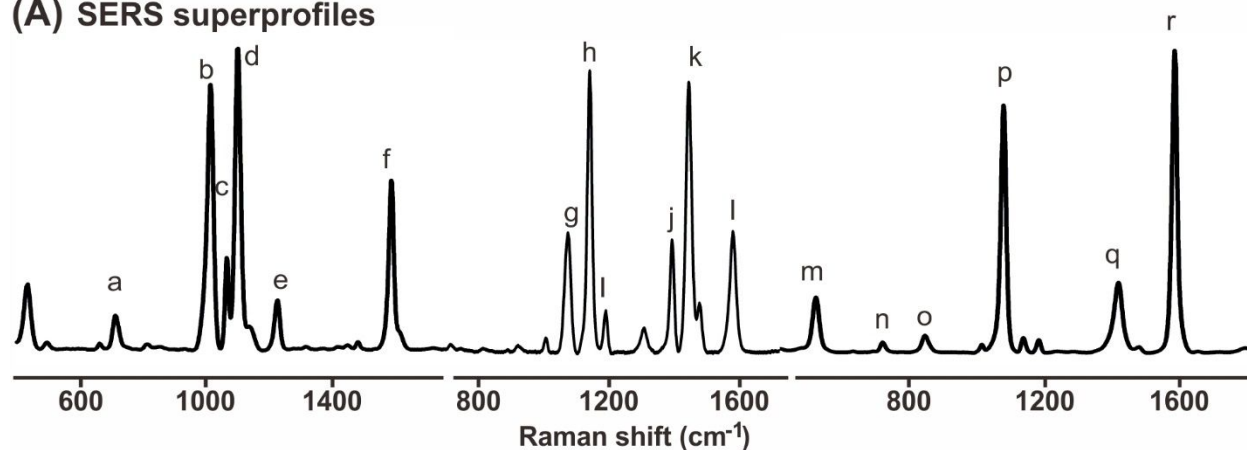


Figure S2. Characterization of synthesized Ag nanocubes. (a) SEM image of the Ag nanocubes. (b) Size distribution of the Ag nanocubes, with edge lengths of 120 ± 5 nm. (c) Extinction spectra of the Ag nanocubes, exhibiting clear plasmonic resonances across the entire visible light region.

(A) SERS superprofiles**(B)**

	Peak position	Experimental (cm ⁻¹)	Assignment
MPY	a	714	$\nu(\text{C-S})$
	b	1014	Ring breathing
	c	1064	$\delta(\text{CH})$
	d	1100	Ring breathing + $\nu(\text{C-S})$
	e	1224	$\beta(\text{CH}) + \delta(\text{NH})$
	f	1586	$\nu(\text{C=C})$ *de-protonated pyridine
ATP	g	1075	$\nu(\text{C=C}) + \nu(\text{C-S})$
	h	1143	$\beta(\text{C-H}) + \nu(\text{C-N})$
	i	1186	$\beta(\text{C-H})$
	j	1393	$\nu(\text{N=N}) + \nu(\text{C-N})$
	k	1441	$\nu(\text{N=N}) + \beta(\text{C-H})$
	l	1580	$\nu(\text{C=C})$
MBA	m	521	$\nu(\text{C-S})$
	n	717	$\gamma(\text{CCC})$
	o	842	$\delta(\text{COO-})$
	p	1077	Ring breathing + $\nu(\text{C-S})$
	q	1418	$\nu(\text{COO-})$
	r	1586	$\nu(\text{C=C})$

ν , stretching; δ , bending; ρ , rocking; β , X-H bending (where X is C, N, O); γ , out of plane bending

Figure S3. SERS super-profile and assigned vibrational modes. (A) A representative SERS super-profile. (B) Vibrational mode assignments for key fingerprints in the super-profile.¹⁻⁶

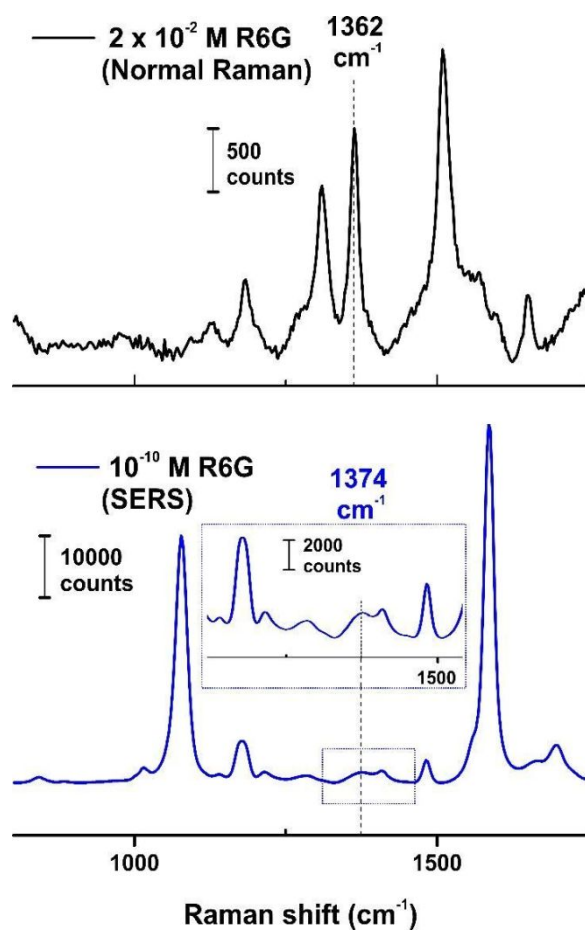


Figure S4. Determining the analytical enhancement factor (AEF) of our SERS sensor using Rhodamine 6G. The normal Raman spectrum of Rhodamine 6G (2×10^{-2} M) drop casted on an aluminum plate is shown in black while the SERS spectra of Rhodamine 6G (10^{-10} M) drop casted on our SERS sensor is shown in blue.

Supplementary Information 1. Calculation of analytical enhancement factor (AEF).

Using Rhodamine 6G (Figure S4),

$$I_{\text{SERS}} = 1269 \pm 44 \text{ counts}$$

$$I_{\text{Raman}} = 1784 \pm 19 \text{ counts}$$

The AEF of our SERS sensor is given as:

$$\begin{aligned} \text{AEF} &= \frac{I_{\text{SERS}}}{I_{\text{Raman}}} \times \frac{C_{\text{Raman}}}{C_{\text{SERS}}} \\ &= \frac{1269}{17.84} \times \frac{2 \times 10^{-2}}{10^{10}} \\ &= 1.4 \times 10^{10} \end{aligned}$$

where C_{SERS} and C_{Raman} are the concentrations of Rhodamine 6G measured using our SERS sensor (10^{-10} M) and normal Raman (2×10^{-2} M) respectively, while I_{SERS} and I_{Raman} are the signal intensities recorded using SERS and normal Raman at their respective concentrations per unit time.

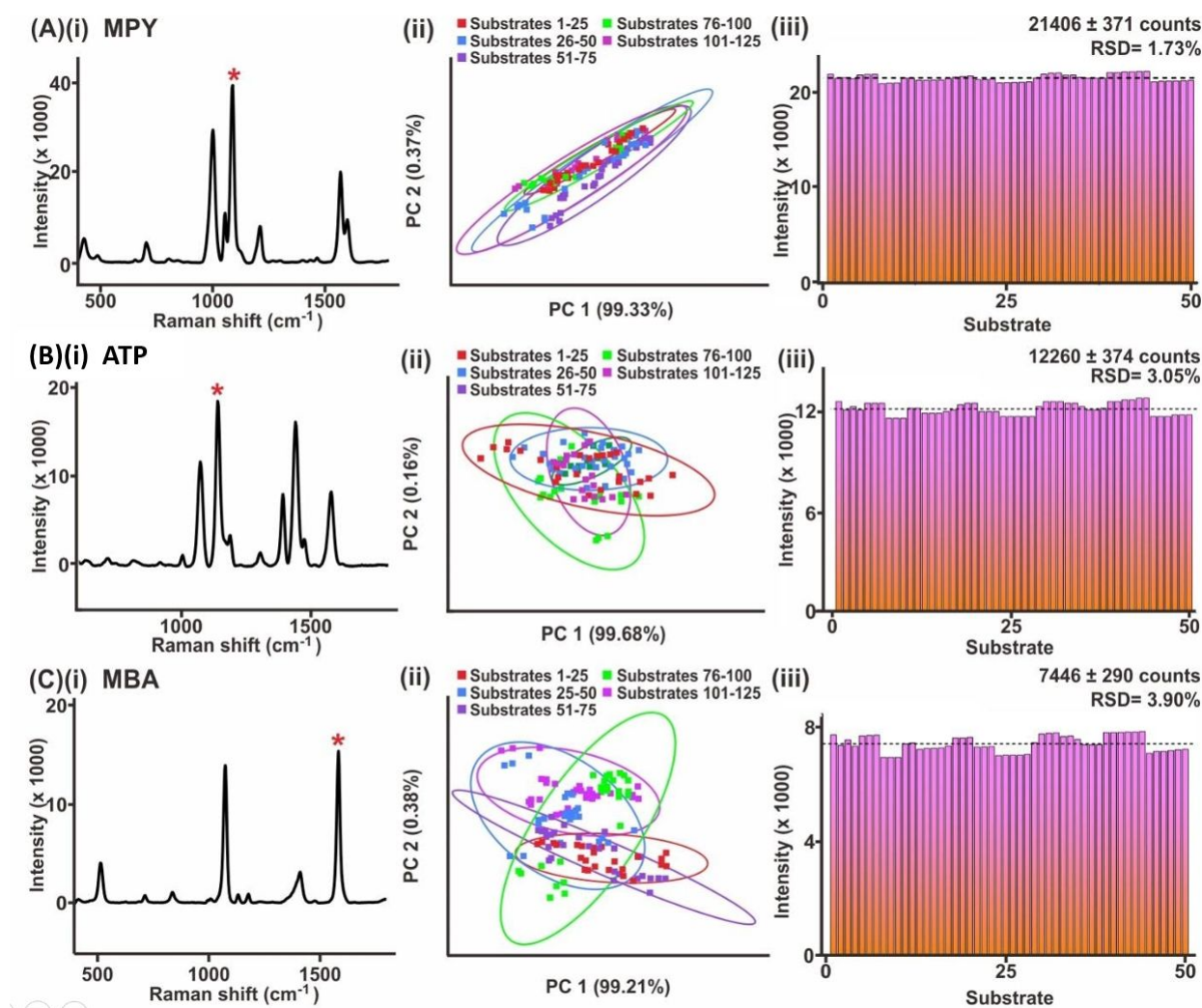


Figure S5. (i) Representative SERS spectra of each molecular receptor. (ii) PCA score plot (PC 1 vs. PC 2) of SERS spectra measured from 125 different sensor chips. The overlap of the spectral clusters indicates that the SERS signals are consistent and reproducible across different chips, with low chip-to-chip variation. (iii) comparison of the SERS intensity homogeneity for 50 different substrates for (A) MPY, (B) ATP, (C) MBA. The respective peak of each probe used to determine the SERS intensity homogeneity is indicated by an '*'.

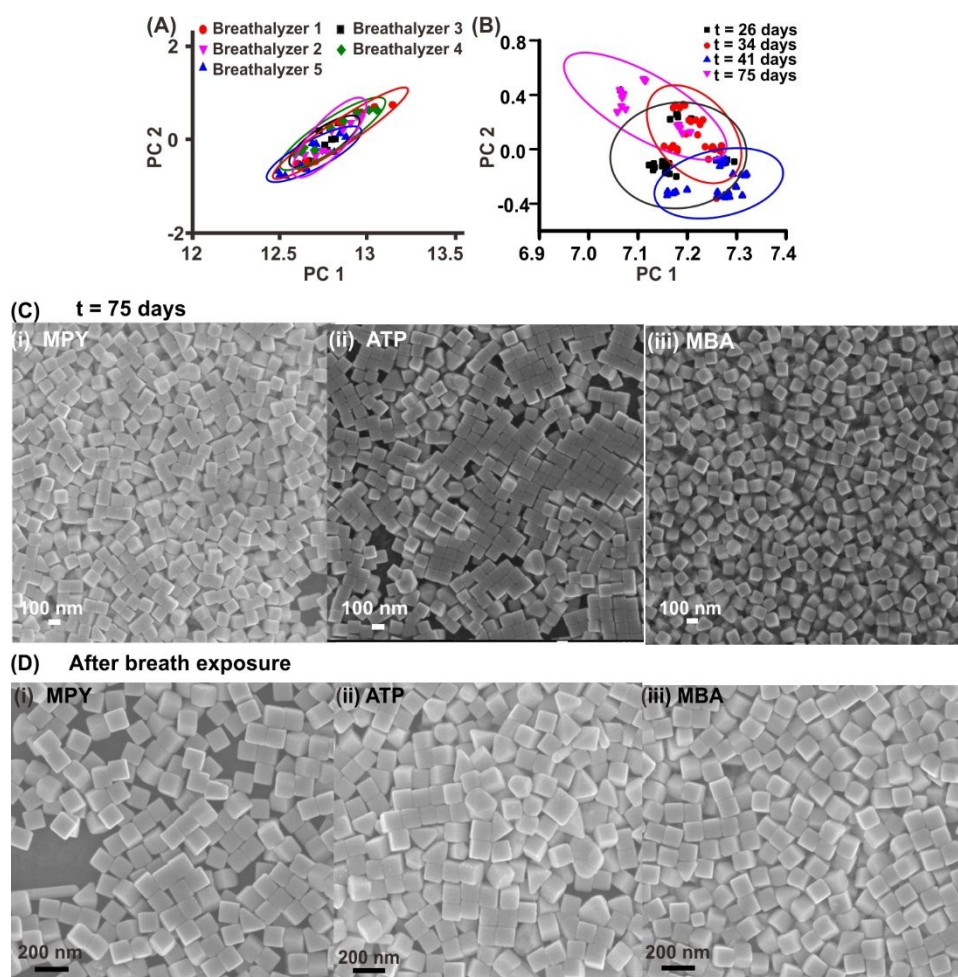


Figure S6. (A) PCA score plot (PC 1 vs. PC 2) of 6 assembled breathalyzers. Close overlap of the individual clusters illustrates the high signal reproducibility across different SERS chips even after breathalyzer integration. (B) PCA score plot (PC 1 vs. PC 2) of five as-fabricated SERS sensor chips at different time durations ($t = 26, 34, 41$ and 75 days) after initial fabrication. Close cluster overlap indicates that the functionalized Ag nanocubes remain chemically stable up to 2.5 months. It is of note that the measured 2.5 months is to affirm the utility of the SERS sensor chips for the duration of the clinical study and does not reflect the maximum shelf-life of the fabricated SERS chip. (C, D) SEM images of sensor chips at (C) $t = 75$ days and (D) after breath exposure for each of the molecular receptors, namely (i) MPY, (ii) ATP and (iii) MBA. The nanocubes maintain their shape integrity with no signs of etching due to oxidation.

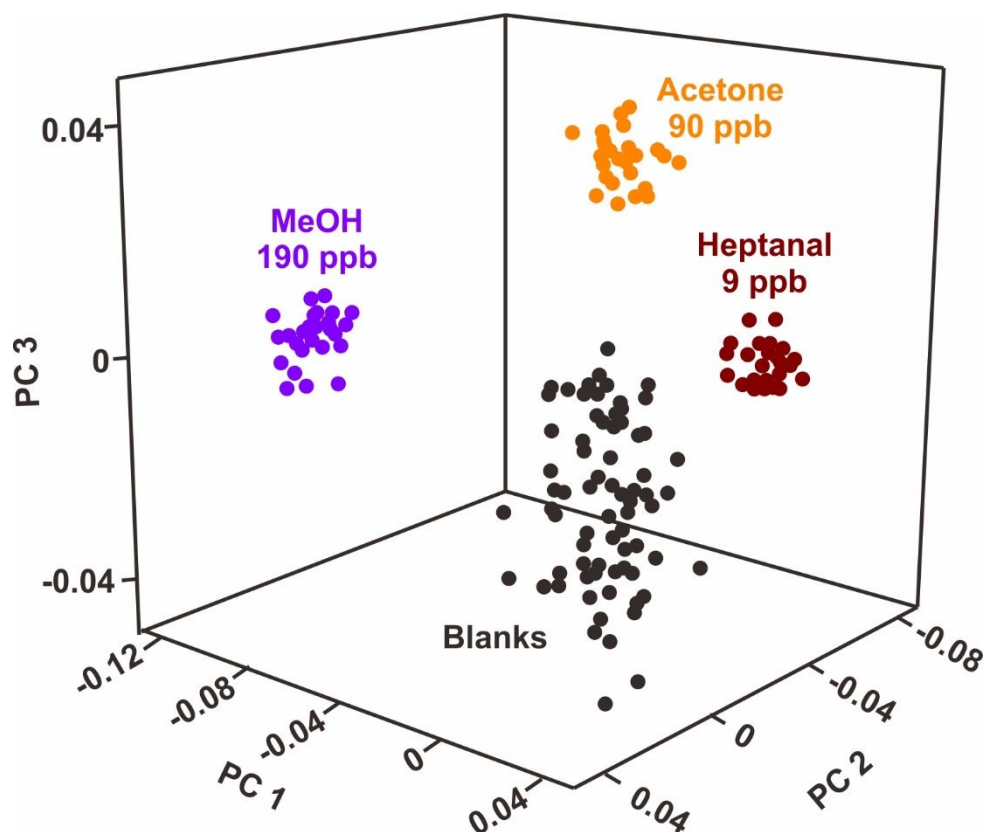


Figure S7. 3D principal component analysis (PCA) score plot (PC1 vs. PC2 vs. PC3) of SERS spectra collected in the absence (blanks) and presence of representative VOC vapors at their respective physiologically relevant levels. Each marker represents a SERS super-profile concatenated from MBA, MPY and ATP SERS spectra. The target VOCs investigated are heptanal (to represent aldehydes), acetone (to represent ketones) and methanol (to represent alcohols). Prior to PCA clustering, the SERS super-profiles are preprocessed using baseline, normalization and general least squares weighting (GLS) to remove clutter variance. The distinct and well-separated spectral clusters illustrate that methanol, acetone and heptanal each induces distinct and unique spectral changes to the receptors' SERS spectra, even at low ppb levels. This demonstrates the sensitivity of our SERS sensor to various VOCs.

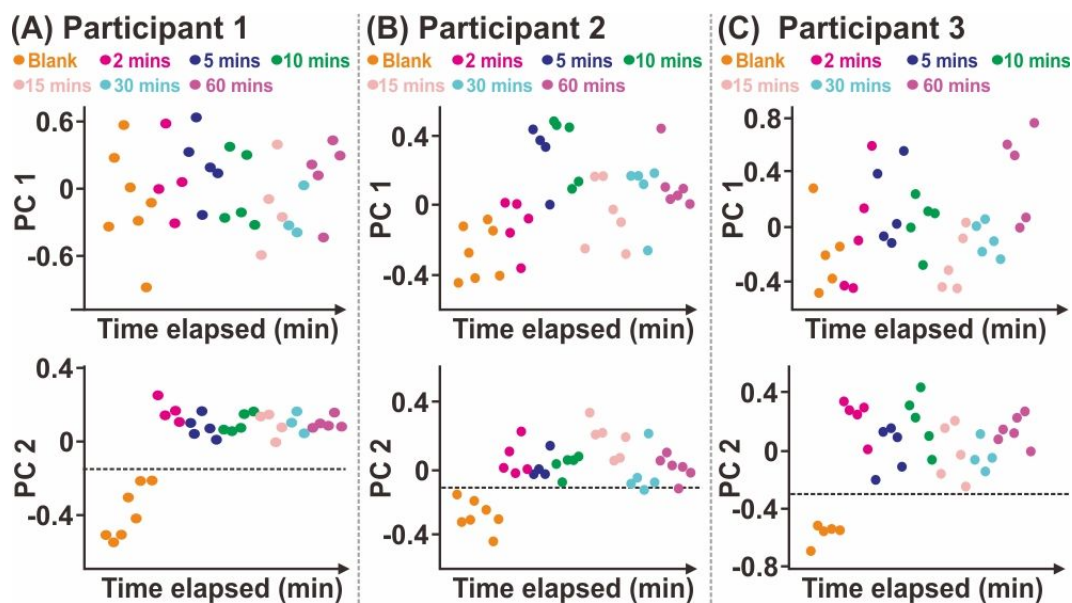


Figure S8. Determination of minimum incubation time for receptor-VOC interactions.

(A-C) PC scores vs. time elapsed after breath exhalation plots for 3 different participants. Upon breath exposure, SERS spectra were measured at fixed time intervals of $t = 2, 5, 10, 15, 30, 60$ and 90 mins. The SERS super-profiles at each time interval were analyzed using principal component analysis and compared with the blank super-profiles. Across all 3 runs, the change in PC 2 score assumes a logarithmic trend, with a distinct change after 2 mins of breath exposure and plateauing at about $t = 60$ mins. The PC 1 scores of all breath samples remains relatively constant throughout, which suggests that breath-induced spectral variation is largely captured in the 2nd PC. Thus, we establish 2 min as the minimum incubation time.

Supplementary Information 2. Calculation of vapor concentrations for pure VOC vapors.

Each SERS sensor is incubated separately with 200 μL of target analyte at 35 $^{\circ}\text{C}$ in an enclosed 20 mL vial. SERS detection was performed after 6h of incubation to allow vaporization to reach an equilibrium state. The saturated vapor concentration (g cm^{-3}) is calculated using the ideal gas equation:

$$PV = nRT$$

where P is the saturated vapor pressure at 35 $^{\circ}\text{C}$ (Pa), V is volume of enclosed vial (cm^3), R is the universal gas constant ($8.314 \times 10^6 \text{ cm}^3 \text{ Pa K}^{-1} \text{ mol}^{-1}$) and T is the incubation temperature (K).

Rearranging the equation,

$$\text{Saturated concentration } (\text{g cm}^{-3}) = \frac{V}{RT} \times \text{MW}$$

Where MW is the molecular weight of the target analyte (g mol^{-1}).

The saturated concentration can be converted from g cm^{-3} to ppm by the following relationship,

$$\text{Saturated concentration (ppm)} = \text{Saturated concentration } (\text{g cm}^{-3}) \times 10^6$$

Table S1. Respective saturated vapor concentrations of each analyte.

Compound	MW (g mol^{-1})	Saturated vapor pressure (Pa)	Saturated vapor concentration (ppm)
ethanal	44.05	143,280	2465
heptanal	100.21	569	22
octanal	128.212	80	4
acetone	58.08	37,519	851
methanol	32.04	21,697	271
water	18.02	5,626	40

Table S2. Summary of test statistics for peak intensity changes among blanks, COVID-positive and COVID-negative.

Comparison	U	Z	Probability > U
MPY 1617 cm ⁻¹ / 1586 cm ⁻¹			
Blank vs. COVID-negative	0	-18.15465	1.17973×10^{-73}
Blank vs. COVID-positive	0	-11.83178	2.67425×10^{-32}
COVID-positive vs. COVID negative	4078	-9.30333	1.36118×10^{-20}
DMAB 1143 cm ⁻¹ / 1075 cm ⁻¹			
Blank vs. COVID-negative	29326	-14.83242	9.04155×10^{-50}
Blank vs. COVID-positive	8771	-2.67483	0.00748
COVID-positive vs. COVID negative	21821	4.79878	1.59638×10^{-6}
DMAB 1186 cm ⁻¹ / 1075 cm ⁻¹			
Blank vs. COVID-negative	4021	-16.44439	9.20048×10^{-61}
Blank vs. COVID-positive	1660	-8.41441	3.94867×10^{-17}
COVID-positive vs. COVID negative	22441	8.2616	2.22045×10^{-16}
DMAB 1393 cm ⁻¹ / 1075 cm ⁻¹			
Blank vs. COVID-negative	48708	-16.49396	4.05455×10^{-61}
Blank vs. COVID-positive	12136	-7.54075	4.67281×10^{-14}
COVID-positive vs. COVID negative	67632	4.20121	2.65494×10^{-5}
DMAB 1441 cm ⁻¹ / 1075 cm ⁻¹			
Blank vs. COVID-negative	32088	-13.89048	7.23536×10^{-44}
Blank vs. COVID-positive	7859	-3.65652	2.55667×10^{-4}
COVID-positive vs. COVID negative	20555	3.67522	2.37645×10^{-4}
MBA 521 cm ⁻¹ / 1077 cm ⁻¹			
Blank vs. COVID-negative	19015	5.71197	1.1678×10^{-8}
Blank vs. COVID-positive	4331	9.54477	1.125×10^{-30}
COVID-positive vs. COVID negative	16276	2.36422	1.807×10^{-2}

Table S3. Comparison of experimental and DFT simulated peak intensities for $\nu(\text{CS})$ mode relative to the ring breathing mode of MBA.

Experimental

	Peak intensity (a.u.)	
	$\nu(\text{CS})$ at 521 cm^{-1} / ring breathing at 1077 cm^{-1}	% Change with analyte incubation
MBA only	0.2451 ± 0.0318	-
MBA-acetone	0.2111 ± 0.0202	-13.91 %
MBA-ethanal	0.1601 ± 0.006	-34.71 %
MBA-heptanal	0.2445 ± 0.0170	-0.28 %
MBA-octanal	0.2160 ± 0.0109	-11.91 %
MBA-MeOH	0.2659 ± 0.0323	+8.45 %
MBA-water	0.3063 ± 0.0061	+24.95 %

DFT simulated

	Peak intensity (a.u.)			
	$\nu(\text{CS})$ at 296 cm^{-1}	Ring breathing at 1099 cm^{-1}	$\nu(\text{CS})$ / ring breathing	% Change with analyte
MBA only	648.8	4053.4	0.1600	-
MBA-acetone	35125.1	222790.5	0.1577	-1.48 %
MBA-ethanal	34160.4	216723.4	0.1576	-1.50 %
MBA-heptanal	38964.9	244067.1	0.1596	-0.23 %
MBA-octanal	25947.8	228943	0.1133	-29.17 %
MBA-MeOH	46121.9	218295.6	0.2113	+32.03 %
MBA-water	29796.6	167335.1	0.1781	+11.27 %

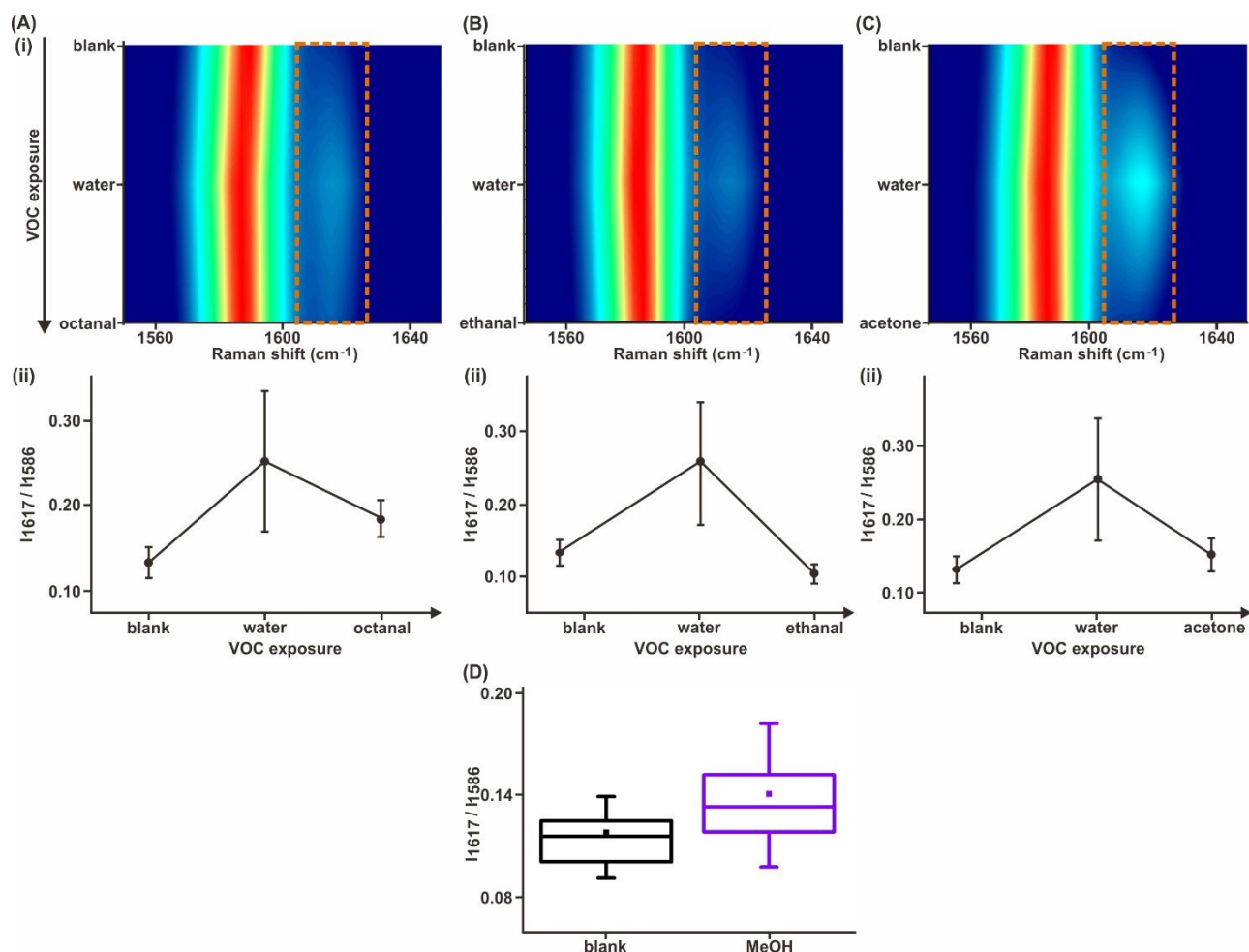


Figure S9. Additional MPY spectral analysis of pure analyte vapors. (A-C) (i) Evolution of 1550 – 1650 cm⁻¹ spectral region, normalized to the 1586 cm⁻¹ peak intensity upon exposure to water vapor and with subsequent exposure to (A) octanal, (B) ethanal, and (C) acetone. (ii) Corresponding $I_{1617\text{cm}^{-1}}/I_{1586\text{cm}^{-1}}$ peak intensity ratios at different stages of exposure. (D) Box plot of $I_{1617\text{cm}^{-1}}/I_{1586\text{cm}^{-1}}$ peak intensity ratios before and after MeOH exposure.

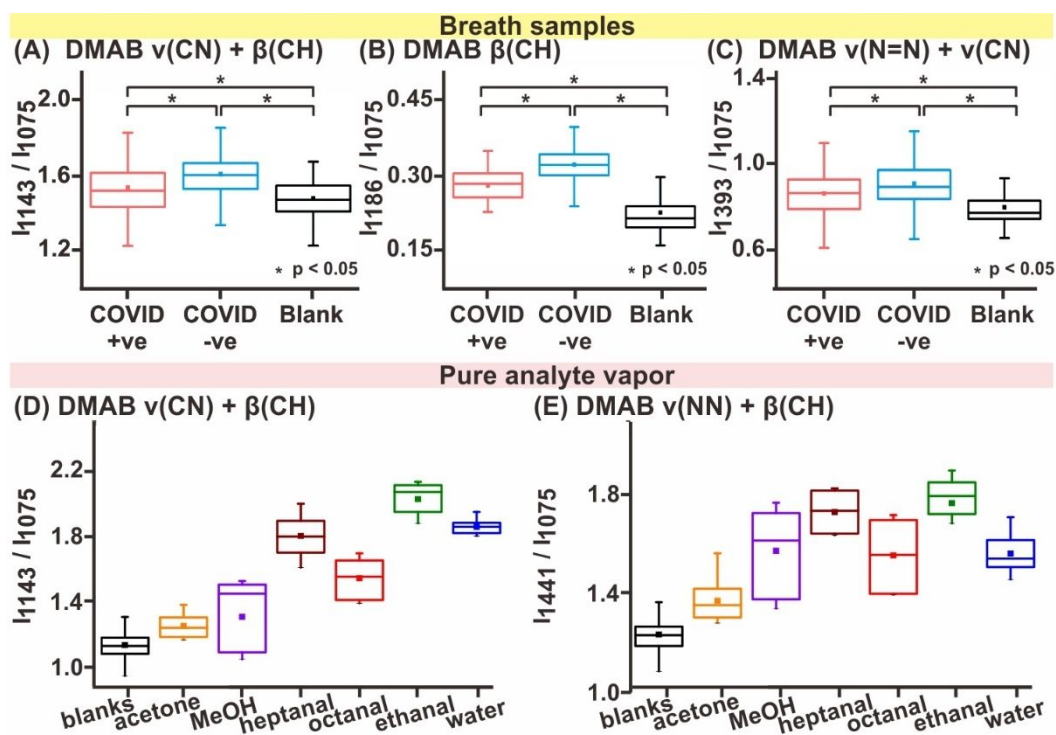


Figure S10. Additional ATP spectral analysis of collected breath samples and pure analyte vapors. (A-C) Boxplots comparing peak intensity ratios between blanks, COVID-positive and COVID-negative samples. (D-E) Boxplots comparing peak intensity ratios between blanks and the respective pure analyte vapor.

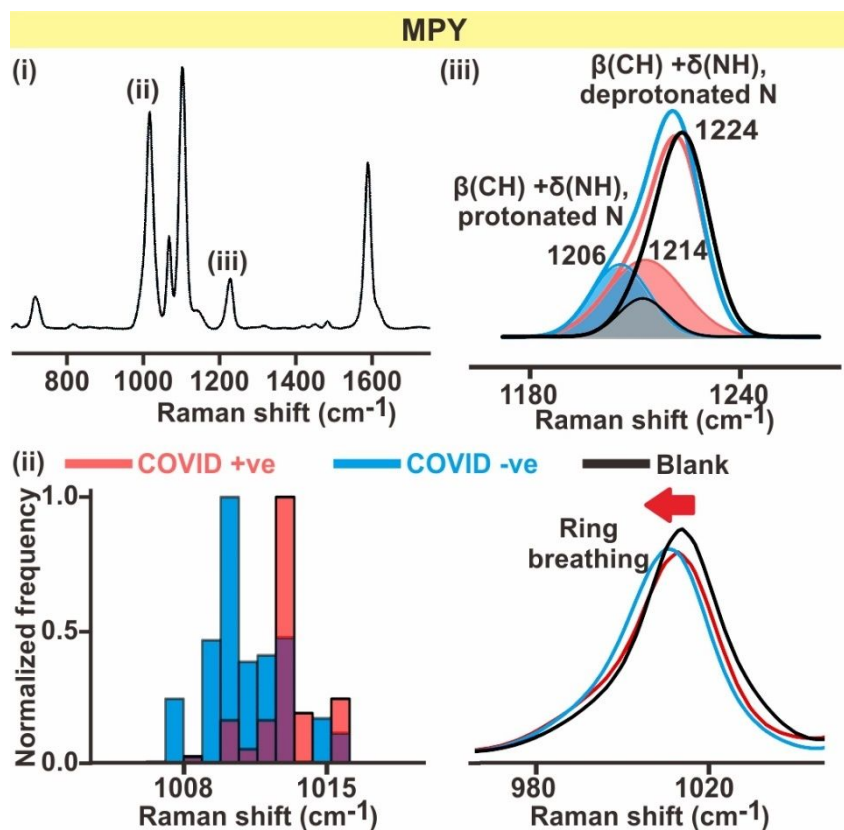


Figure S11. MPY spectral differences. (i) Representative MPY SERS spectra. Peaks of statistical difference between COVID-positive and COVID-negative individuals are indicated by (ii) – (iii). (ii) MPY ring breathing mode indexed at 1014 cm^{-1} red-shifts upon breath exposure, with COVID-negative individuals exhibiting a larger red-shift in general, as indicated by the histogram (left). (iii) COVID-negative individuals cause a larger intensification of the shoulder peak indexed to CH bending coupled with NH bending $\beta(\text{CH}) + \delta(\text{NH})$ with protonated N compared to COVID-positive individuals.

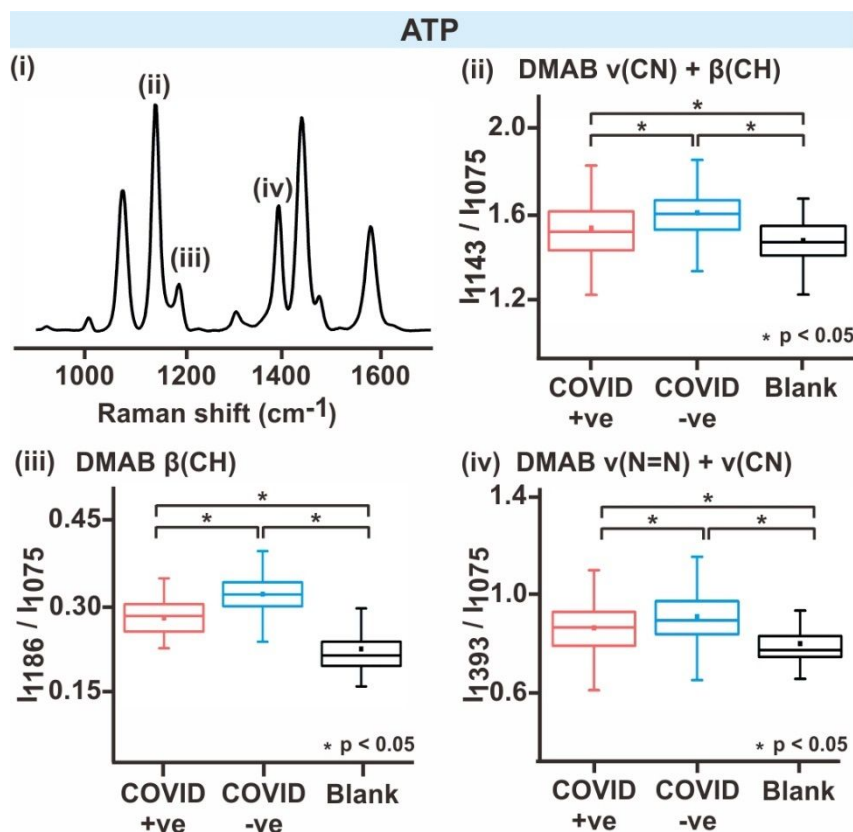


Figure S12. ATP spectral differences. (i) Representative ATP SERS spectra. Peaks of statistical difference between COVID-positive and COVID-negative individuals are indicated by (ii) – (iv). As discussed in the main text, ATP is known to undergo laser-induced dimerization to form DMAB, with characteristic DMAB peaks observed at 1143, 1186 and 1393 cm^{-1} . (ii-iv) Boxplots comparing peak intensity ratios between blanks, COVID-positive and COVID-negative samples for (ii) DMAB CN stretching coupled with CH stretching $\nu(\text{CH})$, (iii) DMAB CH bending $\beta(\text{CH})$ and (iv) DMAB CN stretching coupled with N=N stretching $\nu(\text{NN})$. As highlighted in the main text, the DMAB-associated peaks intensify upon breath exposure, with COVID-negative samples inducing a larger increase than COVID-positive samples. All statistical significances, determined by the Mann-Whitney rank sum test at $p < 0.05$ level, is indicated by *. For all box plots, the mean and median are represented by the square box symbol and horizontal line respectively. The main box covers the lower to upper quartiles while the whiskers are extended to cover all data points that lie within ± 1.5 interquartile range.

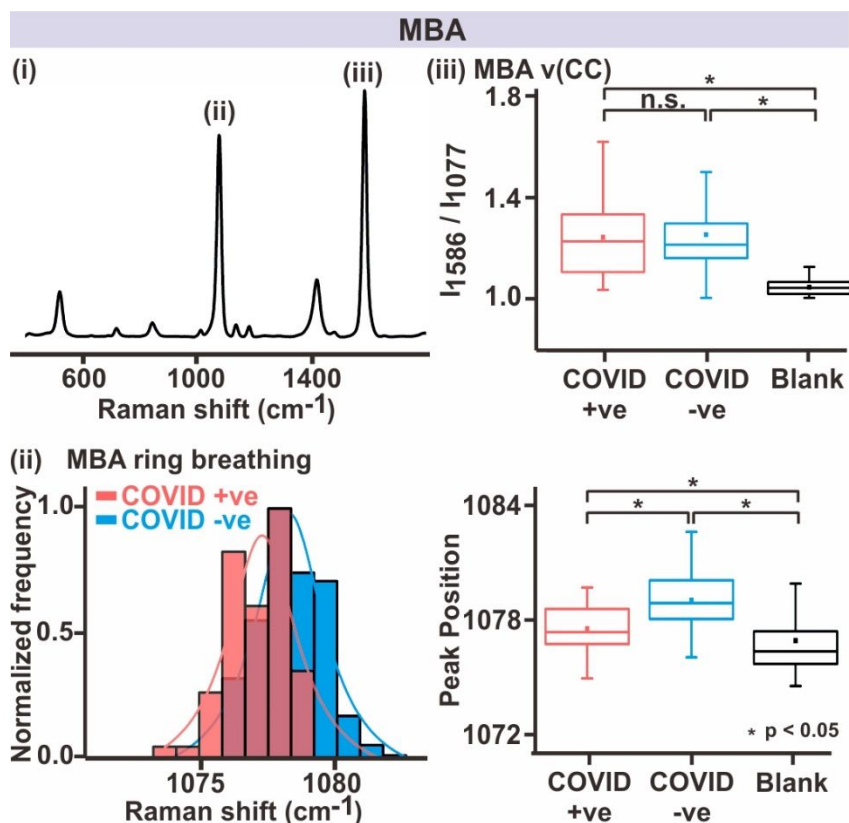


Figure S13. MBA spectral differences. (i) Representative MBA SERS spectra. Spectral regions that undergo changes upon breath exposure are indicated by (ii) – (iv). (ii) COVID-positive samples cause an increase in intensity of MBA COO⁻ bending $\delta(\text{COO}^-)$ mode indexed at 842 cm⁻¹ while there are negligible changes for COVID-negative samples. (iii) MBA ring breathing mode indexed at 1077 cm⁻¹ blue-shifts upon breath exposure, with COVID-negative individuals exhibiting a larger blue-shift in general, as indicated by the histogram (left). (iv) MBA CC stretching $\nu(\text{CC})$ mode indexed at 1486 cm⁻¹ intensifies upon breath exposure. However, there are negligible differences between COVID-positive and COVID-negative samples, as denoted by n.s. All statistical significances, determined by the Mann-Whitney rank sum test at $p < 0.05$ level, is indicated by *. For all box plots, the mean and median are represented by the square box symbol and horizontal line respectively. The main box covers the lower to upper quartiles while the whiskers are extended to cover all data points that lie within ± 1.5 interquartile range.

Table S4. Sensitivity and specificity metrics for each of the 50 PLSDA iterations.

Model no.	Sensitivity (%)	Specificity (%)
1	89.19	100
2	100	100
3	100	100
4	97.3	99.07
5	94.59	100
6	100	100
7	94.59	99.53
8	91.89	100
9	100	100
10	91.89	100
11	91.89	100
12	93.33	100
13	100	100
14	91.89	100
15	100	100
16	94.59	100
17	97.3	99.53
18	100	100
19	94.59	100
20	100	100
21	94.59	100
22	97.3	99.07
23	100	100
24	100	100
25	97.3	100
26	97.3	100
27	97.3	100
28	91.89	100
29	100	100
30	97.3	100
31	94.59	100
32	91.89	100
33	97.3	100
34	94.59	100
35	100	100
36	94.59	100
37	97.3	100
38	93.33	100
39	91.89	100
40	100	99.53
41	94.59	100
42	100	100
43	97.3	100
44	100	100
45	100	100
46	86.49	100
47	94.59	100
48	94.59	100
49	100	100
50	89.19	100

Supplementary Information 3. Sample calculation of a model sensitivity and specificity.

	Actual PCR Positive	Actual PCR Negative
Predicted Positive	71	0
Predicted Negative	3	427

$$\begin{aligned}\text{Sensitivity} &= \frac{\text{True Positive}}{\text{True Positive} + \text{False Negative}} \\ &= \frac{71}{71 + 3} \times 100\% \\ &= 96\%\end{aligned}$$

$$\begin{aligned}\text{Specificity} &= \frac{\text{True Negative}}{\text{True Negative} + \text{False Positive}} \\ &= \frac{427}{427 + 0} \times 100\% \\ &= 100\%\end{aligned}$$

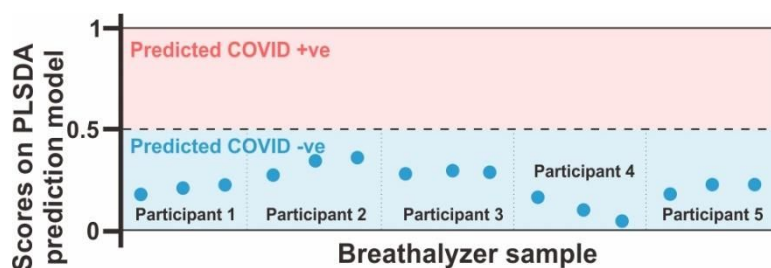


Figure S14. PLS-DA classification scores and outcomes across 5 participants. 3 breath samples were collected from each participant as replicates.

We affirm the reproducibility of our model by conducting a small laboratory-based replicate study with 5 COVID -ve volunteers (not included in the 501 sample size). Their predicted classification outcomes using 3 separate breath samples are all consistent and predicted correctly as COVID -ve. Hence, this affirms that our classification model provides reproducible and consistent results.

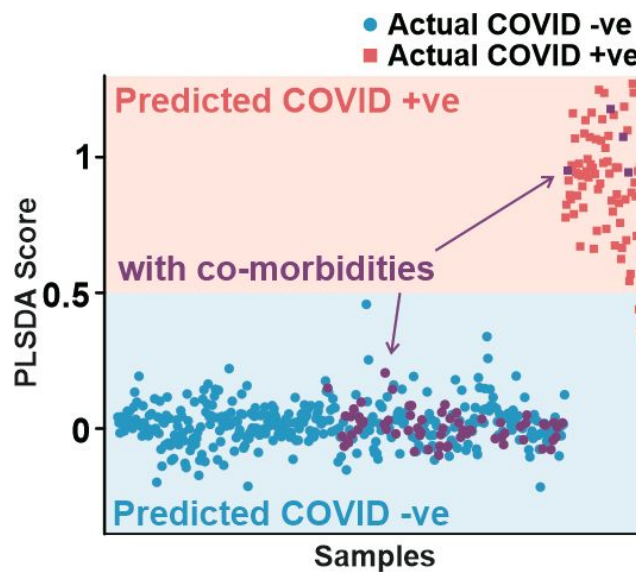


Figure S15. PLSDA score plot derived from the classification of individual SERS super-profiles. Participants with reported comorbidities are highlighted in purple, illustrating that the participants' existing health conditions do not affect their classification scores.

We would like to highlight that since the provision of this information is strictly voluntary, we do not have the information for all 501 trial participants. Nonetheless, the accurate classification of the 70 participants with reported comorbidities indicates that our SERS sensor is able to identify specific differences in participants' breath profiles that were directly linked to whether they had COVID-19 or not.

References

1. Chen, L.; Sun, H.; Zhao, Y.; Zhang, Y.; Wang, Y.; Liu, Y.; Zhang, X.; Jiang, Y.; Hua, Z.; Yang, J., Plasmonic-Induced SERS Enhancement of Shell-Dependent Ag@Cu₂O Core–Shell Nanoparticles. *RSC Adv.* **2017**, *7*, 16553-16560.
2. Hu, J.; Zhao, B.; Xu, W.; Li, B.; Fan, Y., Surface-Enhanced Raman Spectroscopy Study on the Structure Changes of 4-Mercaptopyridine Adsorbed on Silver Substrates and Silver Colloids. *Spectrochim. Acta, Part A* **2002**, *58*, 2827-2834.
3. Jiang, L.; You, T.; Yin, P.; Shang, Y.; Zhang, D.; Guo, L.; Yang, S., Surface-Enhanced Raman Scattering Spectra of Adsorbates on Cu₂O Nanospheres: Charge-Transfer and Electromagnetic Enhancement. *Nanoscale* **2013**, *5*, 2784-2789.
4. Sun, F.; Galvan, D. D.; Jain, P.; Yu, Q., Multi-Functional, Thiophenol-Based Surface Chemistry for Surface-Enhanced Raman Spectroscopy. *Chem. Commun.* **2017**, *53*, 4550-4561.
5. Zhang, L.; Weng, Y.-j.; Liu, X.; Gu, W.; Zhang, X.; Han, L., Fe(iii) Mixed IP₆@Au NPs with Enhanced SERS Activity for Detection of 4-ATP. *Sci. Rep.* **2020**, *10*, 5752.
6. Capocéfalo, A.; Mammucari, D.; Brasili, F.; Fasolato, C.; Bordini, F.; Postorino, P.; Domenici, F., Exploring the Potentiality of a SERS-Active pH Nano-Biosensor. *Front. Chem.* **2019**, *7*.